Journal of Molecular Structure 1301 (2024) 137321

Contents lists available at ScienceDirect

Journal of Molecular Structure

journal homepage: www.elsevier.com/locate/molstr

Solid-state synthesis of poultry waste derived hydroxyapatite: Effect of calcination temperature on crystallographic parameters and biomedical competency

Mashrafi Bin Mobarak [a], Md. Najem Uddin [b], Fariha Chowdhury [c], Md. Sahadat Hossain [a], Monika Mahmud [a], Shifa Sarkar [a], Nazmul Islam Tanvir [b], Samina Ahmed [a,b,*]

[a] Institute of Glass and Ceramic Research and Testing (IGCRT), Bangladesh Council of Scientific and Industrial Research (BCSIR), Dhaka 1205, Bangladesh
[b] BCSIR Laboratories Dhaka, Bangladesh Council of Scientific and Industrial Research (BCSIR), Dhaka 1205, Bangladesh
[c] Biomedical and toxicological Research Institute (BTRI), Bangladesh Council of Scientific and Industrial Research (BCSIR), Dhaka 1205, Bangladesh

ARTICLE INFO

Keywords:
Hydroxyapatite
Calcination temperature
Crystallographic analysis
Cytotoxicity
Bioactivity

ABSTRACT

The efficacy of hydroxyapatite (HAp) in a specific application depends on certain characteristics such as crystallographic parameters, phase, morphology, dimensional anisotropy, particle size, etc. The calcination temperature plays a crucial role in these properties, and selecting the optimum temperature for the intended application is very crucial. In this study, HAp was produced using eggshell of chicken, a type of poultry waste. The synthesis was carried out using the solid-state method. Subsequently, the material was subjected to calcination at three different temperatures: 750 °C, 850 °C, and 950 °C. The prepared S-HAp samples underwent characterization through XRD, FTIR, Raman, FESEM, EDX, DLS particle size (hydrodynamic diameter), and zeta potential. Crystallographic parameters, such as crystallite size (CS), degree of crystallinity (CI), lattice measurements, density of dislocations, micro-strain, and the proportions of β-TCP in terms of percentage and volume, were also calculated. CS was calculated using five methods and CI was estimated using XRD, FTIR and Raman data. The biomedical competency of S-HAp samples in terms of cytotoxicity, hemolysis, antibacterial activity and bioactivity was investigated. Variance in crystallographic parameters with respect to calcination temperature was observed, although variance in biomedical competency was insignificant. The S-HAp samples synthesized using poultry waste were found to be highly biocompatible, bioactive, and antibacterial as well.

1. Introduction

The endeavor of deciphering the construction of natural bone started centenaries aback, followed by gradual understanding and success upon exploration. Calcium phosphates, the hierarchical building blocks of the bone, are structured in a lamellar or layer-by-layer manner [1]. The applicability of calcium phosphate ceramics was first proposed in 1920 by Albee and Morrison, who observed rapid bone growth while treating bone defects [2,3]. Six years later, in 1926, Dejong identified the mineral phase of hydroxyapatite (HAp) as the constituent of bone, which pioneered the exploration of synthetic HAp as a replacement for bone as well as other biomedical applications [4,5]. In 1958, Posner et al. made significant advancements in terms of the crystallographic structure determination of HAp acquired from chemical precipitation [6]. Analyzing the HAp crystallographic properties is a very ancient yet crucial approach.

HAp, the major inorganic constituent that accounts for 65–70 % of bone, has gained the terminology of ``bio-material'' on account of its sublime bio-compatibility and excellent interaction with bone, even under sluggish conditions [7]. Owing to such, HAp has generated significant attention in the field of biomedicine, i.e., implantation or prostheses in orthopedics, maxillofacial and dental surgery, reparation or substitution of hard tissues [8–10]. Apart from biomedical applications, HAp is also used in areas such as chromatography, catalysis, gas sensing, environmental remediation, etc. [11–13]. The synthesis of high-quality HAp with appropriate biocompatible qualities is currently the subject of extensive research, as is the hunt for cost-effective, non-polluting production techniques [14]. The processes that are frequently employed for HAp synthesis include chemical precipitation [15], sol–gel [16], hydrothermal [17], solid-state [18], microwave

* Corresponding author.
E-mail address: shanta_samina@yahoo.com (S. Ahmed).

https://doi.org/10.1016/j.molstruc.2023.137321
Received 31 October 2023; Received in revised form 12 December 2023; Accepted 14 December 2023
Available online 14 December 2023

irradiation [19], UV radiation [20], gamma radiation [21]. All these reported techniques have their own demerits; for instance, chemical precipitation entails a specific pH value, which is usually high; potential for phosphate hydrolysis and the costly nature of raw materials are two disadvantages of the sol–gel process; limited implementation of the hydrothermal process due to inadequate morphology control [22]. Conversely, the solid-state technique is commonly employed to produce a diverse array of materials through the interaction of powdered substances with high-energy ceramic grinding media within mills. Due to its rapid reaction time, relatively low temperature demands, and potential to yield materials with distinct characteristics, this approach has been utilized for many years to generate metastable crystalline and amorphous phases, along with nanostructured materials. Such outcomes are unattainable with traditional methods [23].

Waste-utilized synthesis of HAp is a well-known technique that is widely accepted in the scientific community. The major wastes that are being utilized for HAp synthesis include mammalian (bovine, camel, horse, pig bone, etc.), marine (fish bone and scale), shells (egg, mussel, clam shell, etc.), etc. [24]. HAp synthesized from these origins offers the advantage of being cost-effective and readily available. Additionally, it contains minerals like Mg, K, Na, and Zn, enhancing its bioactivity, osteoconductivity and osseointegration of bone regeneration [25,26]. Among these wastes, eggshell is the 15th biggest food industry pollution issue, and improper disposal of this waste poses a health risk owing to fungal growth on the eggshells [27]. About 9–12 % of an egg's weight is made up of its shell, and this shell contains about 94–97 % of $CaCO_3$, which makes it an excellent source of Ca for the synthesis of HAp [12].

Herein, solid-state synthesis of HAp was carried out utilizing waste chicken eggshell (WCE), and calcination was done at three different temperatures. The impact of varying calcination temperatures on properties, particularly crystallographic parameters, was examined. Furthermore, the influence of temperature on the biomedical performance of the synthesized S-HAp samples, including cytotoxicity, hemolysis, bioactivity, and antibacterial activity, was studied. All samples exhibited noteworthy biomedical effectiveness with minor distinctions, rendering them suitable for use in biomedical applications.

2. Materials and methods

2.1. Materials

As a source of Ca, WCE was chosen and only the white WCEs were collected, washed, boiled, membrane separated and dried. The dried WCEs were then ball milled to produce fine powder. Di-ammonium hydrogen phosphate (DAHP) was procured form E. Merck, Germany. All the chemicals utilized were of analytical quality and were employed without any additional processing.

2.2. Methods

2.2.1. Synthesis of hydroxyapatite

Solid-state route was followed for the synthesis of HAp as reported in our previous works [12,13,28]. The quantity of Ca and P precursors relies on achieving the theoretical Ca/P ratio of 1.67. Considering that the batch of WCE contained 95 % $CaCO_3$, a mixture of 40 g of WCE powder and 30 g of DAHP was used based on this composition. This mixture underwent ball milling at a speed of 450 revolutions per minute for a duration of 6 h. The ball milled powder was split into three segments, each of which underwent calcination at temperatures of 750 °C, 850 °C, and 950 °C for 30 min, with a gradual temperature increase of 5 °C per minute. The S-HAp samples were labelled as S-HAp750, S-HAp850, S-HAp950 and stored air tightly. The reaction involving the solid-state route is shown below and the synthesis procedure is illustrated in Fig. 1.

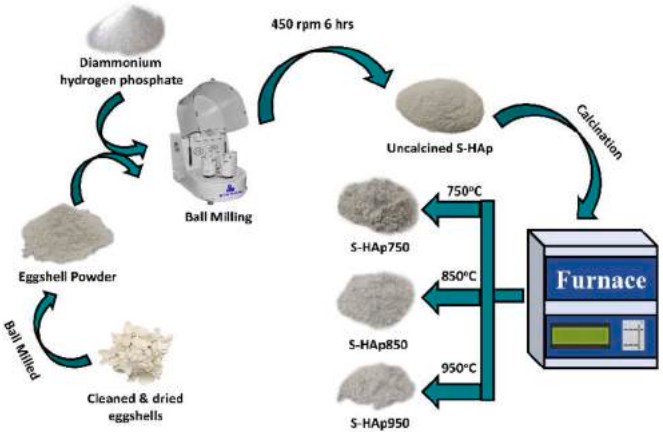

Fig. 1. Synthesis procedure of HAp by solid-state route.

$$10\ CaCO_3 + 6\ (NH_4)_2HPO_4 \xrightarrow{\text{Calcination}} (1-x)Ca_{10}(PO_4)_2(OH)_2 + 3xCa_3(PO_4)_2 \quad (1)$$

2.2.2. Characterization techniques

Different characterization techniques were employed to assess the characteristics of the synthesized S-HAp samples (S-HAp750, S-HAp850 and S-HAp950). Firstly, confirmation of HAp phase was done with X-ray powder diffractometry (Rigaku Smart Lab XRD, scan range 5° to 70°, scanning rate 30°/min, CuKα radiation with wavelength of 1.54060 Å, voltage and current of 40 kV and 50 mA respectively and the fixing step was 0.01°). FTIR (Fourier-transform infrared spectroscopy using an IR Prestige21 instrument with MIRacle10 ATR) and Raman spectroscopy (performed using the HORIBA Macro-RAM™ system) were conducted to analyze functional groups. Examination of morphology and elemental composition were done with field-emission scanning electron microscopy (FESEM) and energy-dispersive X-ray spectroscopy (EDX) (operating conditions: accelerating voltage 15 kV; probe current 1 nA and energy range 0–20 keV) with a JEOL JSM-7610F instrument. For assessing hydrodynamic diameter and zeta potential, dynamic light scattering (DLS) was performed using a Malvern Panalytical Zetasizer Ultra particle size analyzer.

2.2.3. Determination of crystallite size (CS)

For crystalline materials, the distinction between ``crystallite size'' and ``particle size'' is crucial. XRD is regarded as an effective and potent instrument for determining the size of crystallites [29]. Four different methods based on the XRD data was exploited for determining the CS of the synthesized S-HAp samples [30]. Table 1 represents the methods, equations and the calculation techniques for CS.

2.2.4. Determination of crystallinity index (CI)

Crystallinity is an important property to consider when selecting HAp for biomedical applications, since it is directly related to the bioactive response. CI gives the quantitative measurement of crystallinity and hence, the crystallinity index of S-HAp750, S-HAp850 and S-HAp950 was measured. CI was measured using three techniques: XRD, FTIR and Raman data and the calculations were based on the following equations [34,35],

$$CI = X_s = \left(\frac{K_a}{\beta_{(211)}}\right)^3 \quad (2)$$

$$CI = CI_{XRD} = \sum \frac{H_{(2\ 0\ 2)} + H_{(3\ 0\ 0)} + H_{(1\ 1\ 2)}}{H_{(1\ 2\ 1)}} \quad (3)$$

Table 1
Crystallite size calculation of S-HAp750, S-HAp850, S-HAp950 by four different methods.

No.	Method	Equation (rearranged)	Plot	CS calculation	Ref.
1.	Monshi–Scherrer (M–S)	$\ln\beta = \ln\frac{k\lambda}{D} + \ln\frac{1}{\cos\theta}$	$\ln\frac{1}{\cos\theta}$ (x axis) $\ln\beta$ (y axis)	$\ln\frac{k\lambda}{D}$ = Intercept	[31]
2.	Halder–Wagner (H–W)	$\left(\frac{\beta}{\tan\theta}\right)^2 = \frac{K\lambda}{D}\frac{\beta\cos\theta}{\sin^2\theta} + 16\varepsilon^2$	$\frac{\beta\cos\theta}{\sin^2\theta}$ (x axis) $\left(\frac{\beta}{\tan\theta}\right)^2$ (y axis)	$\frac{K\lambda}{D}$ = Slope	[32]
3.	Williamson–Hall (W–H)	$\beta.\cos\theta = \frac{K\lambda}{D} + 4\varepsilon\sin\theta$	$4\sin\theta$ (x axis) $\beta\ .\ \cos\theta$ (y axis)	$\frac{K\lambda}{D}$ = Intercept	[33]
4.	Size-strain plot (SSP)	$(d\beta\cos\theta)^2 = \frac{K\lambda}{D} \times (d^2\beta\cos\theta) + \frac{\varepsilon^2}{4}$	$d^2\beta\cos\theta$ (x axis) $(d\beta\cos\theta)^2$ (y axis)	$\frac{K\lambda}{D}$ = Slope	[32]

Here, β = full width half maxima (FWHM); K = Scherrer's constant also known as shape factor (0.9); λ is the wavelength of X-ray (0.154060 nm); D = crystallite size (nm); d = interplanar distance or d-spacing; ε = micro-strain.

$$CI = X_C = 1 - \frac{V_{112/300}}{I_{300}} \quad (4)$$

$$CI = CI_{FTIR-Height} = \frac{A_{603} + A_{567}}{A_{590}} \quad (5)$$

$$CI = CI_{FTIR-Absorbance} = \frac{Ab_{1030}}{Ab_{1020}} \quad (6)$$

$$CI = CI_{Raman} = FWHM_{960} \quad (7)$$

Here, K_a = constant = 0.24, $\beta_{(211)}$ indicates full width half maximum (FWHM) at the (211) plane. The heights of the peaks at the (202), (300), (112), and (121) planes are represented by $H_{(2\ 0\ 2)}$, $H_{(3\ 0\ 0)}$, $H_{(1\ 1\ 2)}$, and $H_{(1\ 2\ 1)}$ respectively. $V_{112/300}$ stands for the intensity in the valley between the (112) and (300) planes. The intensity of the (300) plane is designated as I_{300}. Furthermore, A_{603}, A_{567}, and A_{590} signify the absorbance of FTIR peaks at wavenumber positions 603, 567, and 590 cm^{-1}. Ab_{1030} and Ab_{1020} refer to the absorbance of FTIR peaks at positions 1020 and 1030 cm^{-1}. Lastly, $FWHM_{960}$ corresponds to the FWHM at the Raman shift of 960 cm^{-1}.

2.2.5. Bioactivity study

The assessment of the bioactivity of the produced S-HAp750, S-HAp850, and S-HAp950 was conducted by observing the development of apatite within simulated body fluid (SBF). The process entails placing the S-HAp samples into a simulated body fluid (SBF) solution and keeping them at 37 °C within an incubator for a duration of 21 days. Prior to and subsequent to immersion in SBF, FESEM images were captured. The SBF solution, with a pH of 7.4, was prepared using the method previously documented. [36].

2.2.6. Cytotoxicity test

The cytocompatibility of the S-HAp samples were assessed following the Trypan blue exclusion test reported elsewhere [20,21,37]. The cytotoxic response of hydroxyapatite was observed in Vero Cell line (CLS 605372, Germany) of kidney epithelial cell (African green monkey). Cell culture was done with Dulbecco's Modified Eagles Medium (DMEM) which was made with 10 % (v/v) fetal bovine serum, 1 % penicillin – streptomycin (100 U mL^{-1}) and 0.1 mg mL^{-1} of neomycin; incubation temperature was maintained at 37 °C with 5 % (v/v) CO_2. The S-HAp samples underwent steam sterilization, and an evaluation was performed using the cultured cell line at three distinct concentrations for each sample (50, 100, and 200 μg/mL). The response of the cell line to the S-HAp samples was monitored over a 72-h period, after which the cell count was performed using an automated cell counter (LUNA-II™, Analytikjena). The identical experiment was repeated three times for every sample, and cell viability was quantified using the subsequent equation,

$$\text{Cell viability} = \frac{\text{Number of live cells}}{\text{Total number of cells}} \times 100\ \% \quad (8)$$

2.2.7. Hemolysis assay

The hemolysis assay of the S-HAp samples was carried out by following the procedure reported by Padmanabhan et al. [38]. With the aid of anti-coagulant heparin, human blood samples were collected and incubated at 37 °C for 1 h. Three concentrations (50, 100 and 200 μg/ml) were chosen for each S-HAp sample and solutions were prepared using sterilized phosphate buffer saline (PBS). All these 9 samples were then mixed with the incubated blood samples (0.4 ml each) and subjected to further incubation for 1 h. Similar procedure was followed except no S-HAp samples were added. In this case, the PBS acted as the negative control and de-ionized water was the positive control. Following the incubation period, the specimens underwent centrifugation at a speed of 5000 rpm for 5 min, and the resulting liquid above the sediment was gathered. Absorbance measurements of these collected liquids were taken at 545 nm using a UV–vis spectrophotometer. This absorbance data depicts the release of hemoglobin as a result of red blood cell lysis and using this phenomenon, following equation helps in calculating the% of hemolysis [39],

$$\%\ \text{Hemolysis} = \frac{D_t - D_{nc}}{D_{pc} - D_{nc}} \times 100 \quad (9)$$

Here, D_t = absorbances of S-HAp test samples, D_{nc} = negative control and D_{pc} = positive control.

2.2.8. Antibacterial study

The antibacterial activity of the S-HAp samples was evaluated against *Staphylococcus aureus* (ATCC 9144) and *Escherichia coli* (ATCC 11303) following the well diffusion method described earlier [40]. Briefly, Mueller–Hinton Broth (MHB) was used for bacterial colony culture where 4 wells of 6 mm diameter were made with sterile micropipette tips. Three of the wells were loaded with 400 μg/ml of S-HAp samples and 5 % dimethyl sulfoxide (DMSO) was put in the remaining well. Kanamycin (30 μg) was also introduced as a positive control. After 24 hrs of incubation, zone of inhibition was calculated.

3. Results and discussion

3.1. X-ray diffraction analysis

Phase composition analysis of the S-HAp samples were conducted using X-ray diffraction. This analysis helped in determining the purity of the HAp phase and its crystallographic as well as structural properties. Fig. 2 depicts the XRD patterns of S-HAp750, S-HAp850, and S-HAp950. The XRD patterns of all the specimens indicated the existence of the HAp phase, as evidenced by the characteristic peaks at 31.8° (211), 32.2° (112), and 32.9° (300). However, a secondary peak was also observed at around 31.06° for S-HAp750, 31.07° for S-HAp850 and 31.10° for S-HAp950, all correspond to the (0210) plane is indicative of the presence of β-tricalcium phosphate (β-TCP) (ICDD PDF card no: 04-006-9376) [28,41]. Upon examining the X-ray diffraction patterns, it became apparent that as the sample was subjected to heating up to 950 °C, the intensity of the HAp peaks progressively amplified. This suggests that the quantity and dimensions of the hexagonal-dipyramidal nanocrystals within the powdered particles expanded with the rising temperature

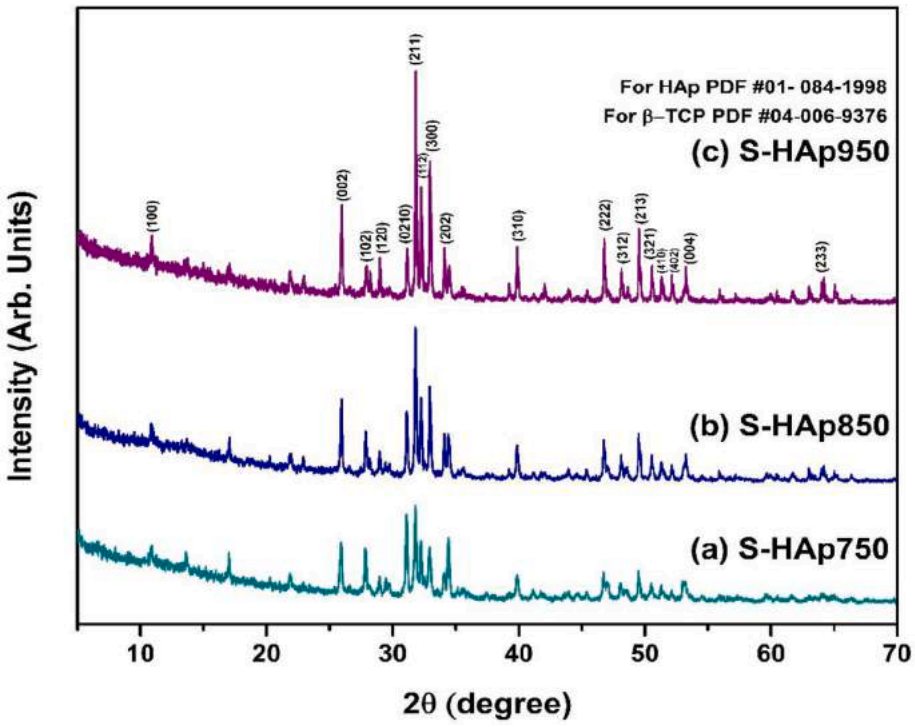

Fig. 2. X-ray diffraction patterns of synthesized S-HAp750, S-HAp850 and S-HAp950.

[42]. The experimental results were juxtaposed with the established JCPDS dataset (card no: 01-084-1998) [43,44].

Using the data acquired from XRD, crucial crystallographic parameters including lattice dimensions, volume of the hexagonal unit cell, average crystallite size, density of dislocations, micro-strain, proportion of HAp and β-TCP, and volume fraction of β-TCP can be computed through the following Eqs. (10)–(17),

$$\frac{1}{d^2} = \frac{4}{3}\left(\frac{h^2+hk+k^2}{a^2}\right) + \frac{l^2}{c^2} \tag{10}$$

$$V = \frac{\sqrt{3}}{2}a^2c \tag{11}$$

$$D = \frac{k\lambda}{\beta\cos\theta} \tag{12}$$

$$\delta = \frac{1}{D^2} \tag{13}$$

$$\varepsilon = \frac{\beta}{4\tan\theta} \tag{14}$$

$$\%\ \text{of HAp} = \frac{I_{HAp\ (2\ 1\ 1)}}{I_{HAp\ (2\ 1\ 1)} + I_{\beta-TCP\ (0\ 2\ 10)}} \times 100 \tag{15}$$

$$\%\ \text{of}\ \beta-\text{TCP} = \frac{I_{\beta-TCP\ (0\ 2\ 10)}}{I_{HAp\ (2\ 1\ 1)} + I_{\beta-TCP\ (0\ 2\ 10)}} \times 100 \tag{16}$$

$$X_B = \frac{PW_B}{1+(P-1)W_B} \tag{17}$$

The expressions for the aforementioned equations can be stated as follows: d denotes the inter planar distance; a, b, c represent the dimensions of the unit cell; h, k, l symbolize the Miller indices; V stands for the volume of the hexagonal HAp unit cell; δ corresponds to the density of dislocations; ε represents the micro-strain; $I_{HAp(211)}$ signifies the intensity of the peak at the (211) plane of HAp, while $I_{\beta\text{-}TCP(0210)}$ signifies the intensity of the peak at the (0210) plane of β-TCP. X_B denotes the proportion of the volume occupied by β-TCP; p is a constant (2.275); W_B represents the calculated percentage of β-TCP. Lattice parameters and JCPDS values are summarized in Table 2, while Table 3 provides the calculated crystallographic values for S-HAp750, S-HAp850, and S-HAp950.

According to Table 3, with increasing calcination temperature, crystallite size, dislocation density and micro-strain decreases. On the other hand, % of HAp increases with decreased volume fraction of β-TCP. The decrease in micro-strain as calcination temperature increases can be attributed to several factors. Higher temperatures promote improved crystallinity by reducing structural defects and lattice distortions, leading to a more ordered crystal structure. The process also encourages the removal of imperfections within the lattice and facilitates the growth of larger crystallites, thereby reducing strain at grain boundaries. Thermal annealing effects during calcination help relieve internal stresses and stabilize the crystal lattice [45,46].

3.2. FTIR analysis

The FTIR analysis verified the existence of significant functional groups in S-HAp, namely PO_4^{3-} and OH^-. In some cases where carbonate containing compounds are used as a precursor, detection of CO_3^{2-} group is also important as it reflects the integrity of synthesized HAp. The FTIR spectrum of S-HAp750, S-HAp850 and S-HAp950 are presented in Fig. 3. The verification of HAp formation is mainly established through the detection of PO_4^{3-} group which had three main bands in the infrared spectrum; at around 560 cm^{-1}, 600 cm^{-1} and 1000–1100 cm^{-1} [22]. The band observed at approximately 1022 cm^{-1} aligned with the asymmetric stretching vibration (ν_3), while the bands ranging from 560 to 600 cm^{-1} matched the bending vibration (ν_4) of the PO_4^{3-} group [28]. Less intense band was observed at around 960 cm^{-1} which corresponds to the symmetric stretching vibration (ν_1) of PO_4^{3-} group [22].

At higher wavenumber region, all the three S-HAp samples showed bands at 3572 cm^{-1} which can be assigned to the bending mode of OH^- group. Conversely, within the lower wavenumber range, a band at 630 cm^{-1} was detected in all samples with varying intensity, aligning with the bending vibration of the OH^- group [47]. The presence of CO_3^{2-} was

Table 2
Lattice parameters of synthesized S-HAp750, S-HAp850 and S-HAp950.

Material	Lattice dimension (ICDD reference code 01-084-1998)	Lattice dimension (Experimental)
S-HAp750	$a = b = 9.42$ Å $c = 6.87$ Å $V = 527.91$ Å^3	$a = b = 9.42$ Å $c = 6.88$ Å $V = 527.99$ Å^3
S-HAp850		$a = b = 9.41$ Å $c = 6.87$ Å $V = 527.11$ Å^3
S-HAp950		$a = b = 9.40$ Å $c = 6.86$ Å $V = 525.84$ Å^3

Table 3
Crystallographic parameters of S-HAp750, S-HAp850 and S-HAp950.

Parameters	S-HAp750	S-HAp850	S-HAp950
Crystallite size (nm)			
For HAp	56.97	90.77	101.74
For β-TCP	57.66	65.96	64.93
Average Crystallite size: HAp + β-TCP (nm)	57.32	78.37	83.34
Dislocation Density ($\times 10^{-3}$ lines/nm^2)	0.29	0.12	0.09
Micro-strain	0.13	0.08	0.07
% of HAp	57.55	70.40	79.52
% of β-TCP	42.45	29.60	20.48
Volume fraction of β-TCP	2.11	1.08	0.63

observed by the detection of bands at the wavenumbers of ~1420 cm^{-1} (B type) and ~873 cm^{-1} (A type) which are denoted as the carbonyl stretching modes from the CO_3^{2-} group [48,49]. Although presence of such minute scale of CO_3^{2-} is hard to detect through XRD, existence of such increases the solubility of HAp which has been observed via *in-vivo* and *in-vitro* experiments [22]. No broad bands were observed at the wavenumber region 3300–3600 cm^{-1} for all the three samples, meaning the absence of adsorbed H_2O.

3.3. Raman analysis

Raman spectroscopy was exploited to analyze the S-HAp samples which had been calcined at three different temperatures. The objective of the analysis was to investigate the Raman spectral shifts of the functional groups within the sample and to confirm the presence of apatite phase. In addition, the crystallinity of materials which have been produced under different reaction conditions, especially for HAp, can be evaluated using this spectroscopic technique. This data can be utilized to comprehend the influence of reaction conditions on the material's structure and characteristics [50].

Fig. 4 shows the Raman spectrum of the synthesized S-HAp samples (calcined at 750, 850 and 950 °C). The most intense and sharpest peak which is typical for the apatite phase was detected at ~965 cm^{-1} for all three samples. This peak is attributed to the symmetric stretching vibration (ν_1) of the PO_4^{3-} group. The intensity of this peak grew alongside the rise in calcination temperature, a trend that has been documented in earlier literature as well [51]. The stretching vibration of asymmetric P-O bonds (ν_3) was identified within the range of approximately 1049 to 1079 cm^{-1} [52,53]. The other peaks to be mentioned are O-P-O symmetrical bending (ν_2) found at around ~435 cm^{-1} and triplet degenerate vibration, also termed as anti-symmetrical bending (ν_4) vibrations observed within 581 cm^{-1} to 611 cm^{-1} [54–56].

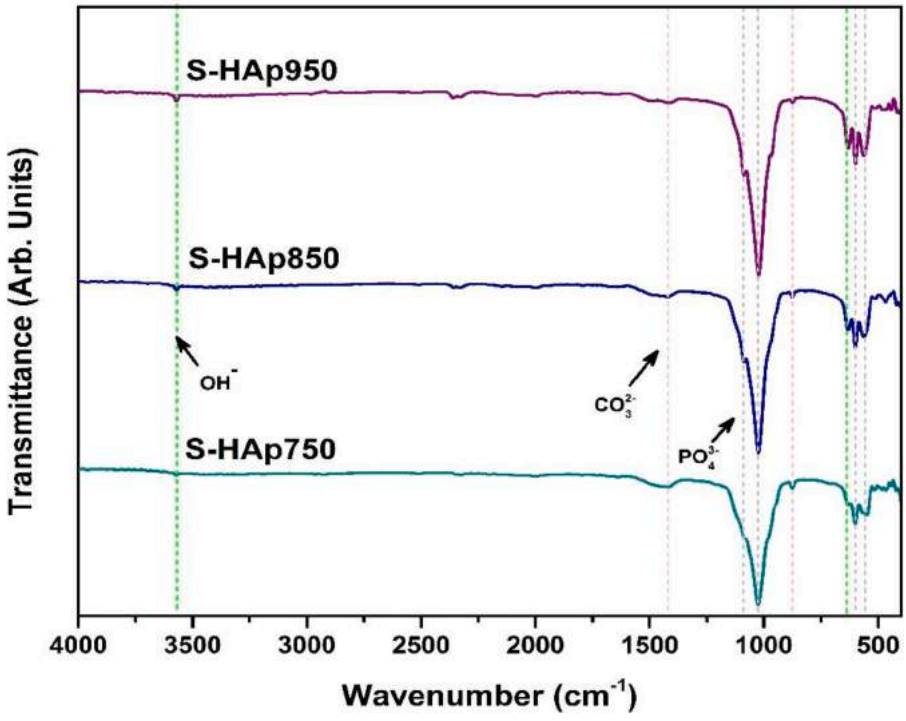

Fig. 3. FTIR spectrum of synthesized S-HAp750, S-HAp850 and S-HAp950.

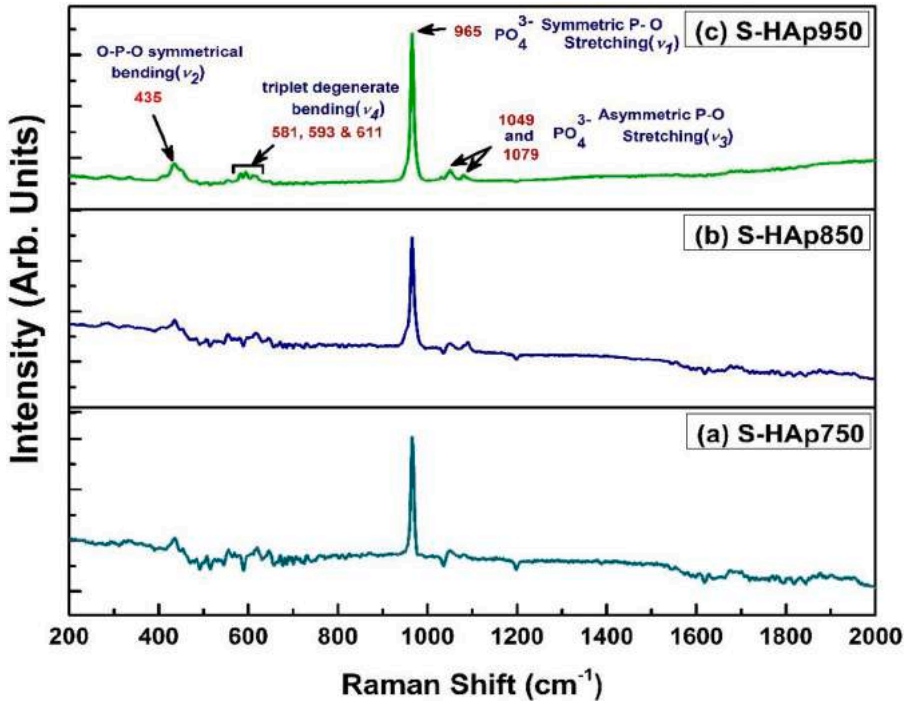

Fig. 4. Raman spectra of the synthesized S-HAp samples.

3.4. CS estimation

Typically, the term "crystallite size" refers to the coherent volume of a substance for a particular diffraction peak. It also relates to the grain size for a powdered sample, and to the thickness for polycrystalline thin films [57]. The size of the crystallites is a significant aspect that impacts the physical attributes of materials, particularly nano-materials. CS must be carefully controlled when creating materials with certain qualities. Since CS is correlated with the broadening of the diffraction peak, information on CS can be obtained using XRD technique [58]. The use of the Scherrer equation (shown in Eq. (12)) is the most well-known technique for determining the CS. Apart from Scherrer equation, four different methods were used to determine the CS of S-HAp samples: Monshi–Scherrer (M–S), Halder–Wagner (H–W), Williamson–Hall (W–H) and Size-Strain Plot (SSP) method. Table 1 represents the corresponding equations and crystallite size calculation techniques of these methods. Details about this estimation is available in our earlier publications [28,30,59].

Plots of the exploited methods is presented in Fig. 5 and the values obtained are tabulated in table 4.

Different XRD based methods typically yield different CS, and it is unclear whether or not the reported deviations are meaningful. Simultaneously, there is no consensus on the benefits and drawbacks of various XRD techniques for determining the CS [58]. So, for picking the best method for CS estimation, the highest value of correlation coefficient (R^2) was considered (except for the Scherrer equation). The Halder-Wagner (H-W) method had the highest R^2 value for CS determination for all three S-HAp samples. Based on H-W approximation, the crystallite sizes of S-HAp750, S-HAp850, and S-HAp950 were determined to be 52 nm, 55 nm, and 66 nm, respectively, indicating an increase in crystallite size corresponding to the calcination temperature. Previous studies extensively investigated the impact of calcination temperature on the physical-chemical properties and the transition in size from nano to micro of these crystals [60,61]. The observed increase in crystallite size with temperature in HAp derived from bovine bone was attributed to a coalescence phenomenon, supported by XRD, TEM, and SEM analyses [62].

3.5. CI valuation by XRD, FTIR and Raman

The level of arrangement within a crystal, referred to as crystallinity, holds significance in the biomedical uses of HAp. The reduced degree of crystallinity in HAp contributes to enhanced solubility and the capacity to bind proteins, offering potential advantages for applications like bone regeneration and various medical purposes. The degree of crystallinity in a material affects its hardness and density. This implies that alterations in crystallinity can exert a notable influence on the material's mechanical characteristics. When considering HAp, alterations in its crystallinity can result in significant variations in mechanical characteristics of scaffolds [34,63]. CI represents a numerical measure of crystallinity, meaning that it can be used to compare the crystallinity of different materials or the same material under different conditions. It is calculated as the proportion of the crystalline component within a particular sample. Earlier studies have demonstrated that XRD, FTIR and Raman spectroscopy are all methods capable of determining CI [35]. However, biomineralization is an evolving process, leading to fluctuations in the mineral CI over time. Consequently, an examination of the precision, effectiveness, and uniformity of these methods in estimating HAp crystallinity indices across varying mineralization phases is warranted. This will enable researchers to select the most suitable method for their particular experimental subjects. To fulfill this objective, it is necessary to create HAp samples with different CI. CI of the synthesized S-HAp samples were calculated according to Eqs. (2)–(7) and the obtained values are presented in Table 5.

A relationship was made with the average crystallite size (HAp calcined at 750, 850 and 950 °C) and the CI calculated by six different methods (Fig. 6). Except for $CI_{FTIR\text{-}Absorbance}$ and CI_{Raman}, linear fitting of all the relationships had correlation coefficient (R^2) greater than 0.9. The R^2 of linear fitting of average crystallite size vs $CI_{FTIR\text{-}Absorbance}$ and average crystallite size vs CI_{Raman} was 0.609 and 0.591 respectively.

3.6. FESEM analysis

The morphology of the synthesized S-HAp samples was investigated in terms of FESEM analysis and is illustrated in Fig. 7(a, d and g). As

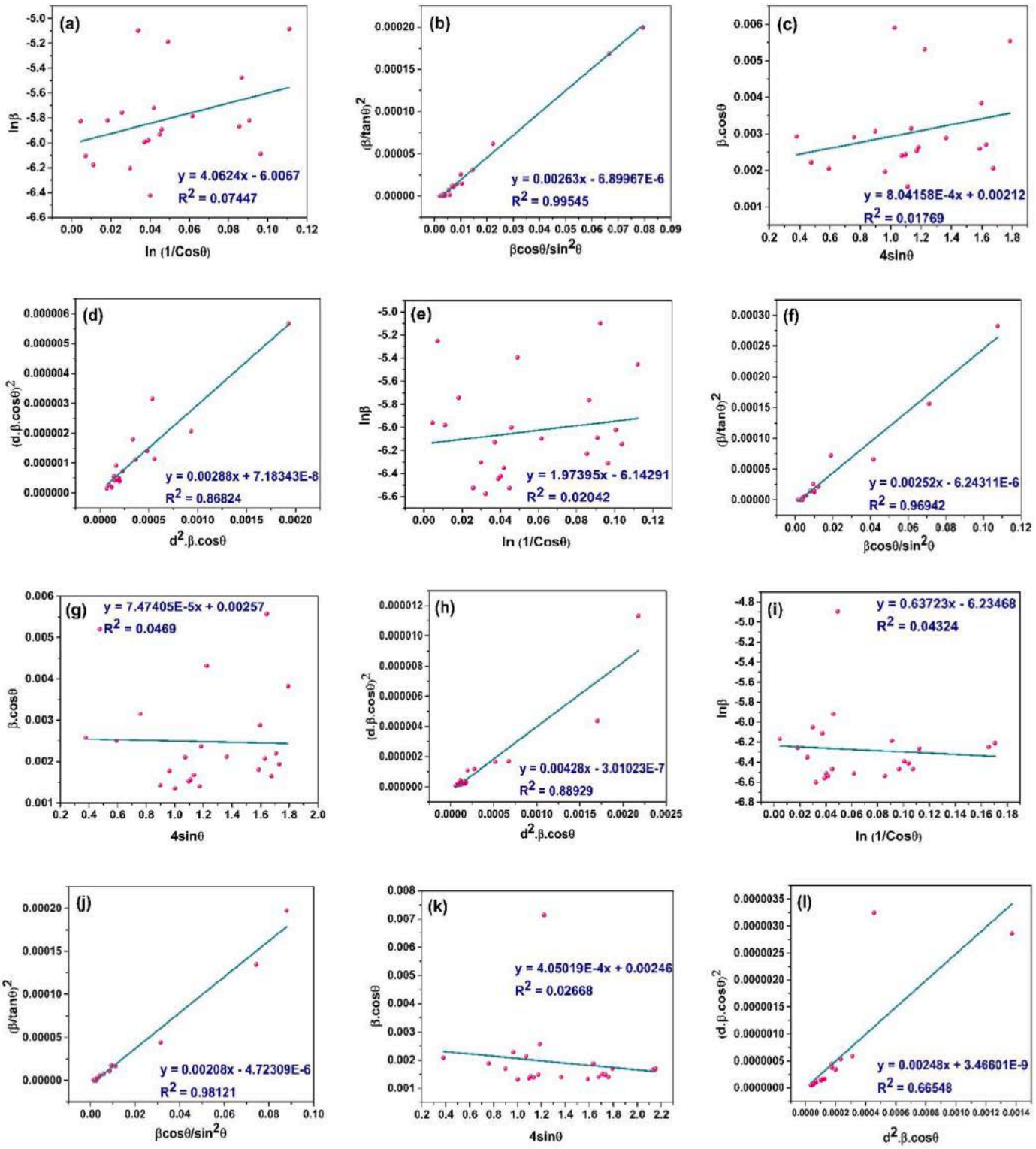

Fig. 5. Crystallite size estimation using Monshi–Scherrer (M–S), Halder–Wagner (H–W), Williamson–Hall (W–H) and Size-Strain Plot (SSP) method respectively: S-HAp750 (a–d); S-HAp850 (e–h); S-HAp950 (i–l).

visualized in the images, S-HAp750 (Fig. 7(a)) has the highest degree of agglomeration and aggregation compared to S-HAp850 (Fig. 7(d)) and S-HAp950 (Fig. 7(g)). All the samples were mainly comprised of plate-shaped flat-type particles as well as irregularly shaped particles. With increasing calcination temperature, the agglomeration as well as aggregation is seen to decrease and particles were more visually separable. This aided in calculating the size (diameter) of the particles using imageJ software following our previously reported procedure [30]. Particles which have visually clear edges were selected for size measurements and shown in Fig. 7(b, e and h). The average particle size for S-HAp750, S-HAp850 and S-HAp950 was found 114±35 nm, 142±38 nm and 190 ± 73 nm. Fig. 7(c, f and i) represents the particle size histograms of the S-HAp samples.

Table 4
Crystallite size estimation using various methods.

No.	Method	S-HAp750		S-HAp850		S-HAp950	
		C.S (nm)	R^2	C.S (nm)	R^2	C.S (nm)	R^2
1.	Scherrer	56	–	90	–	101	–
2.	Monshi–Scherrer (M–S)	56	0.07447	64	0.02042	70	0.04324
3.	Halder–Wagner (H–W)	52	0.99545	55	0.96942	66	0.98121
4.	Williamson–Hall (W–H)	65	0.01769	54	0.0469	56	0.02668
5.	Size-strain plot (SSP)	40	0.86824	32	0.88929	56	0.66548

Table 5
Crystallinity Indices of the S-HAp samples calculated based on XRD, FTIR and Raman spectroscopy.

Sample	Crystallinity index (CI)					
	X_s	X_c	CI_{XRD}	$CI_{FTIR\text{-}Height}$	$CI_{FTIR\text{-}Absorbance}$	CI_{Raman}
S-HAp750	4.53	0.63	1.36	2.99	0.99	9.06
S-HAp850	18.34	0.81	1.18	3.55	1.01	8.60
S-HAp950	24.98	0.86	1.13	3.82	1.04	7.88

3.7. EDX analysis

Fig. 8 provides a visual representation of the elemental composition of S-HAp samples, as determined by EDX analysis. The spectrum illustrates the proportional presence of individual elements, while the mass and weight percentages offer quantifiable details about the conformation. The major elements, Ca (K_a and K_b), P (K_a), and O (K_a), were detected and quantified. The additional peaks in the spectrum were due to the platinum coating and carbon tape substrate, which were not included in the quantification process. The Ca/P ratio was found to be highest for S-HAp750 (1.93) while S-HAp850 and S-HAp950 showed a ratio of 1.49 and 1.76 respectively. These values are 15 % higher for S-HAp750, 10 % lower for S-HAp850 and 5 % higher for S-HAp950 compared to the theoretical Ca/P ratio of HAp which is 1.67. The variation in the Ca/P ratio could arise from the partial substitution of PO_4^{3-} and OH^- ions within the HAp lattice with CO_3^{2-} ions. This is a common occurrence in solid-state and hydrothermal synthesis processes [64].

3.8. DLS hydrodynamic diameter and zeta potential

The hydrodynamic diameter and zeta potential (Fig. 9) of the produced S-HAp samples were measured using a DLS particle size analyzer. The samples were sonicated for one hour in DI water with the solution's natural pH before analysis to lessen the agglomeration of the particles. With an average hydrodynamic diameter of 363 nm, S-HAp750 had the smallest particles, followed by S-HAp850 (441 nm) and S-HAp950 (533 nm). This result is consistent with the FESEM image-based particle size estimation, where S-HAp950 had the largest particle size (190 nm), followed by S-HAp850 (142 nm), and S-HAp750 (114 nm), which had the smallest particle size. The observations show that the hydrodynamic diameter increases with particle size. The zeta potential (also known as electrokinetic potential) of the S-HAp samples were examined to understand the stability of the particles in solution. All the samples showed negative zeta potential value but at different magnitude. The reason behind negative value might be due to the higher sample's pH than their corresponding isoelectric point (pH_{IEP}) or point of zero charge (pH_{PZC}) [65]. Zeta potential was highest for S-HAp950 (−19.28 mV), followed by S-HAp850 (−17.95 mV) and S-HAp750 (−11.11 mV).

3.9. In-vitro studies

3.9.1. Cytotoxicity test

Cytotoxicity refers to a substance's capability to harm or eliminate cells. When a cell encounters a cytotoxic substance, it can undergo different pathways of cell demise, including apoptosis (regulated cell death) and necrosis (cell death due to injury). The results of cytotoxicity assessments are used to determine whether HAp is safe for use in medical applications [66,67]. Fig. 10 represents the cytotoxic response of the

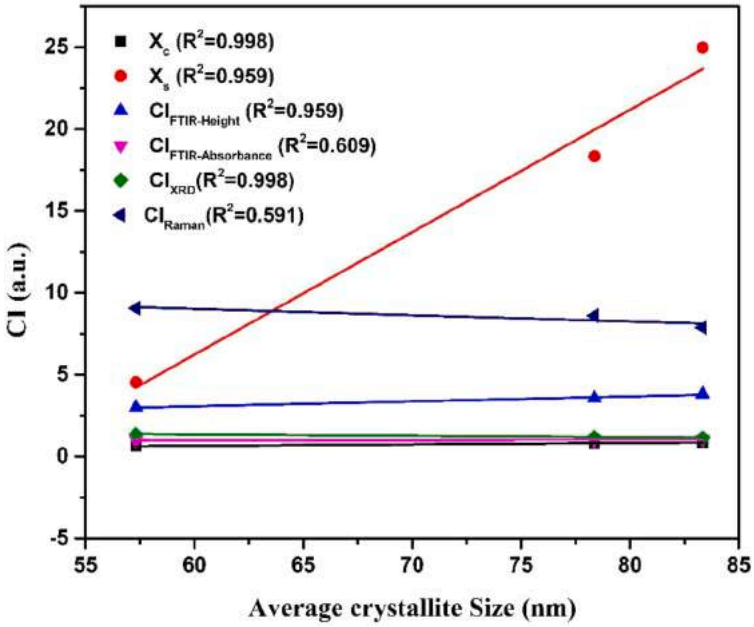

Fig. 6. Relation between average crystallite size and CI calculated by six different methods.

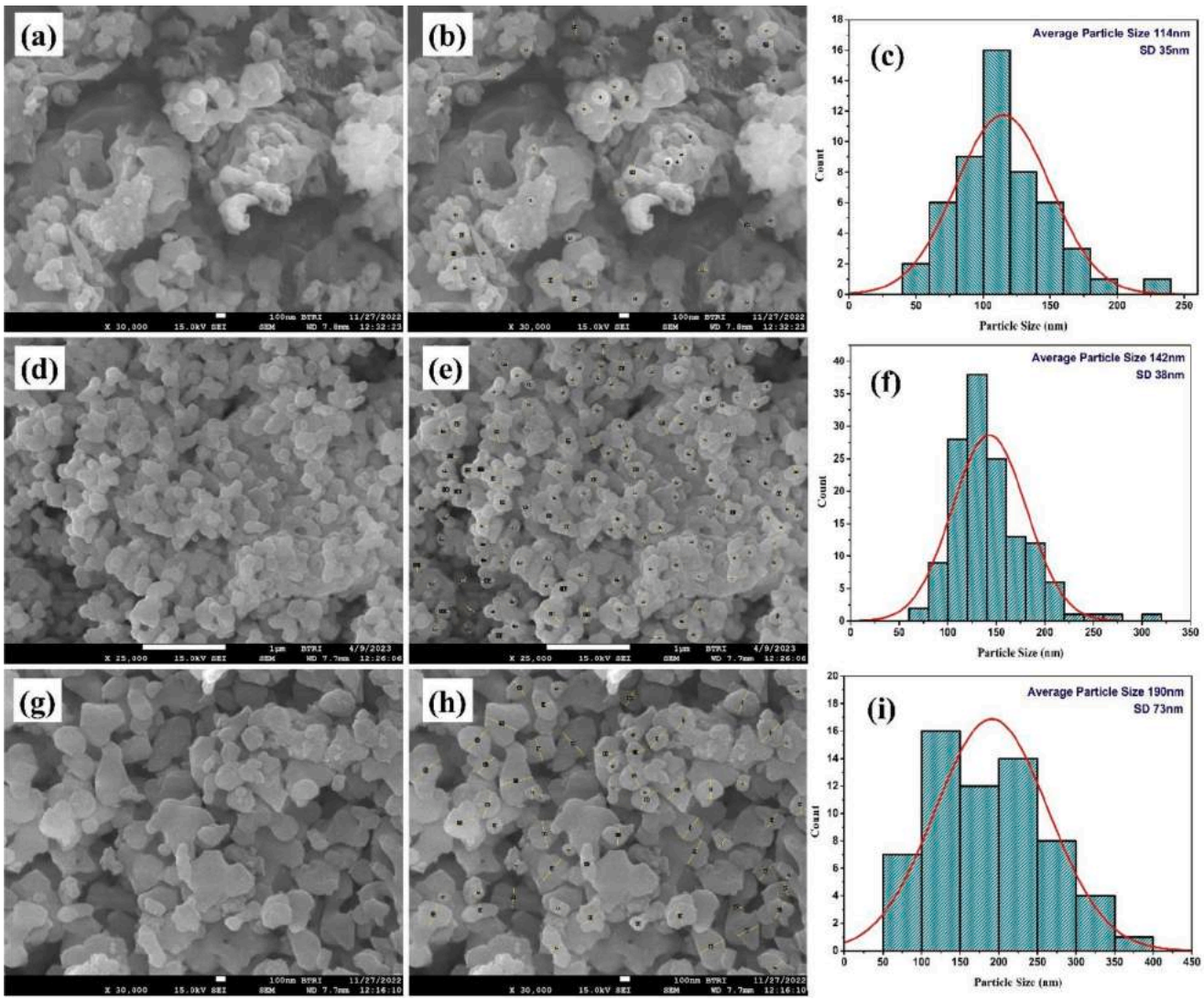

Fig. 7. FESEM image, corresponding particle size selection and particle size histogram of S-HAp750 (a, b and C); S-HAp850 (d, e and f) and S-HAp950 (g, h and i).

synthesized S-HAp samples. The response was observed for three concentrations of each sample and also the control which only contained 5 % DMSO. The utilization of Eq. (8) facilitated the assessment of cell viability in the samples. The produced S-HAp samples exhibited cellular compatibility, as their cell viability exceeded 94 %. This is well above the threshold of 70 % cell viability, which is considered to be the minimum for a material to be considered non-toxic, according to ISO 10993-5:200 [68]. Therefore, the synthesized S-HAp samples are highly cytocompatible. Comparative display of cytotoxic effects (in terms of cell viability %) of S-HAp samples at different concentrations is shown in Fig. 11(a).

3.9.2. *Hemolysis assay*

Hemocompatibility refers to the appropriateness of a material intended for direct interaction with blood [69]. The hemocompatibility of the synthesized S-HAp samples was evaluated and presented in Fig. 11 (b). Three concentrations of each S-HAp sample were tested against blood sample. The results show that, highest% of hemolysis was only 4.4 % exhibited by 200 μg/mL of S-HAp950. The ASTM standard sets a hemolysis rate of less than 5 % as the threshold for highly hemocompatible materials [70]. This result signifies the hemocompatible nature of the S-HAp samples when used in physiological condition and in direct contact with blood.

3.9.3. *Bio-activity study*

Materials like HAp intended for biomaterial applications, such as bone repair, HAp must be able to form apatite in contact with body fluid. The emergence of apatite demonstrates the capacity of the biomaterial to adhere to bone. In this investigation, the bioactivity of S-HAp samples was assessed through their immersion in SBF for a duration of 3 weeks. The FESEM images (Fig. 12) revealed the presence of apatite formation on the surfaces of all samples. Following a 3-week immersion period, the apatite layer was observed to envelop and completely coat the distinct particles across all the samples. This was due to the interaction of the positive and negative charges on the HAp particles and the SBF ions. The combination of these charges led to the nucleation of apatite, which eventually resulted in the supersaturation of the HAp particles with apatite [71]. In simpler terms, the HAp samples were able to bond to the SBF solution and form an apatite layer. This suggests that the HAp samples could be employed as materials for mending bones.

3.9.4. *Antibacterial activity study*

HAp is a gold standard biomaterial with well-documented antibacterial properties. These properties make HAp a valuable material for a variety of medical applications, including implants, wound dressings, and drug delivery systems [21,72–74]. Fig. 13 illustrates antibacterial effectiveness of S-HAp samples against *Staphylococcus aureus* (gram + ve) and *E. coli* (gram -ve), assessed using the well diffusion technique.

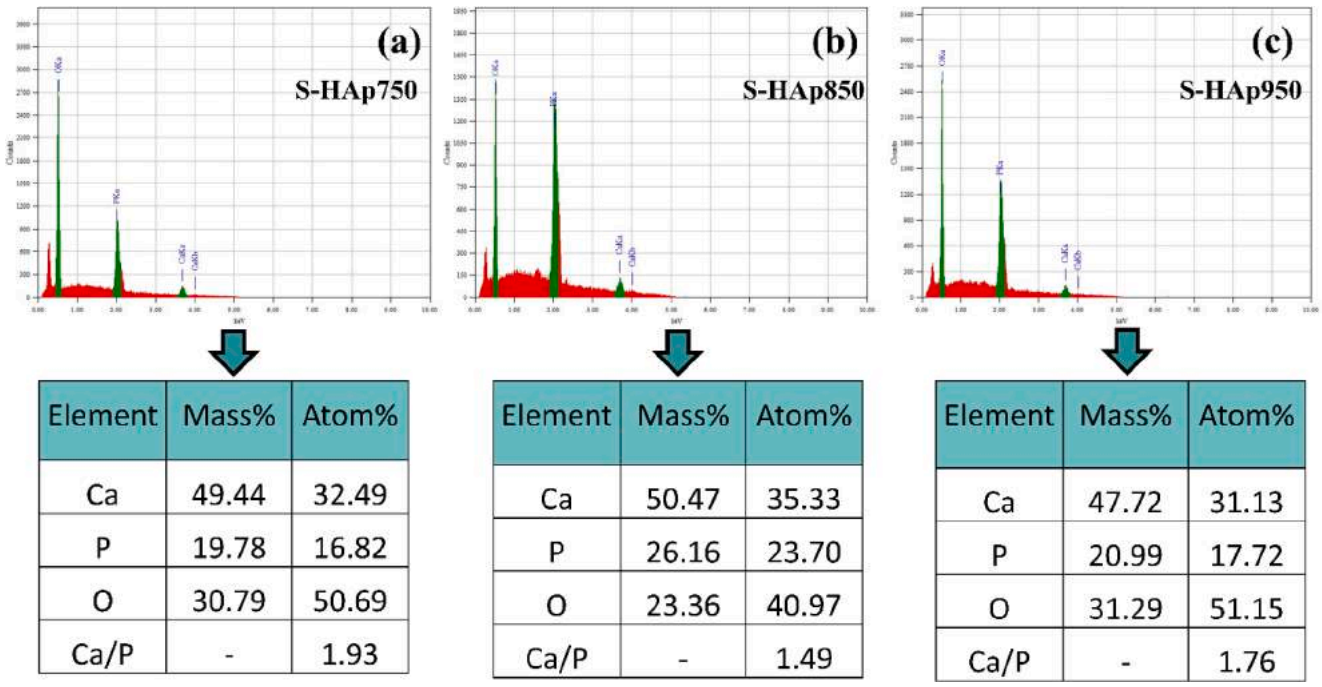

Element	Mass%	Atom%
Ca	49.44	32.49
P	19.78	16.82
O	30.79	50.69
Ca/P	-	1.93

Element	Mass%	Atom%
Ca	50.47	35.33
P	26.16	23.70
O	23.36	40.97
Ca/P	-	1.49

Element	Mass%	Atom%
Ca	47.72	31.13
P	20.99	17.72
O	31.29	51.15
Ca/P	-	1.76

Fig. 8. EDX analysis of (a) S-HAp750, (b) S-HAp850 and (c) S-HAp950.

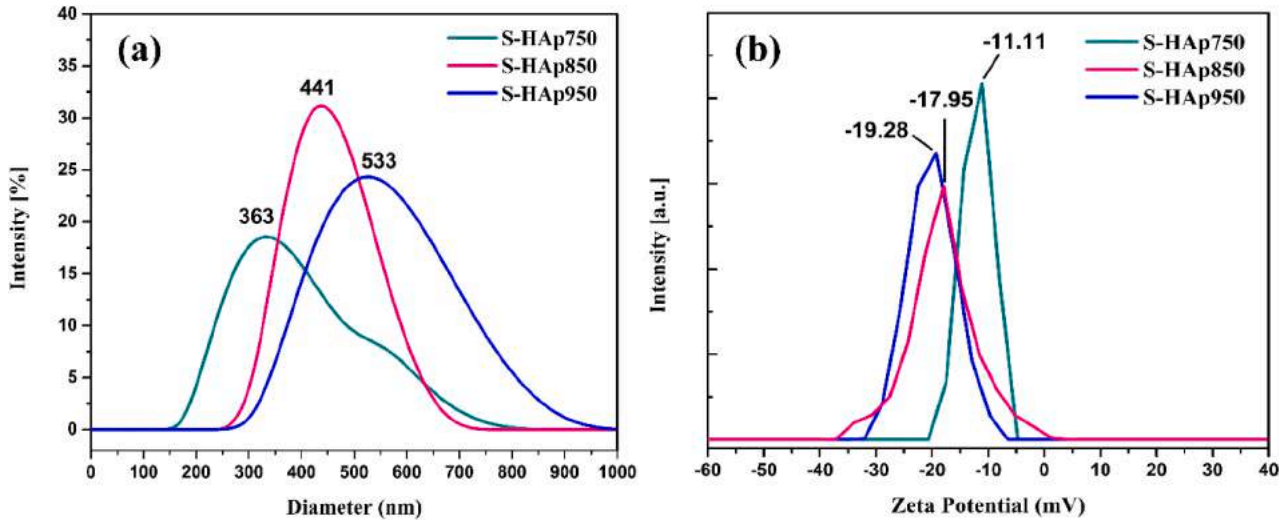

Fig. 9. (a) DLS particle size (hydrodynamic diameter) distribution and (b) zeta potential analysis of S-HAp samples. (solvent = DI water; pH = solution's natural, concentration = 10 μg/ml).

Significant antibacterial activity was shown by the prepared S-HAp samples (400 μg/ml in DMSO) against *S. aureus*, while no discernible activity was observed against *E. coli*. S-HAp750, S-HAp850, and S-HAp950 all had zones of inhibition (ZOI) that were larger than those of the reference (positive control), Kanamycin (30 μg), which had a ZOI of 18 mm. Since *S. aureus*'s infectious effects are mostly responsible for osteomyelitis and other bone-related diseases, S-HAp is a better choice for this treatment due to its anti-*S. aureus* activity [75,76].

4. Conclusion

This work focused on synthesizing HAp by utilizing a waste material through solid-state reaction route. Three different calcination temperature were selected from 750 to 950 °C with an increment of 100 °C and in-vitro studies e.g., cytotoxicity, hemolysis, antibacterial activity and bioactivity of these samples were carried out. This synthesis protocol begets biphasic HAp with varying % of β-TCP alongside. Based on the results obtained, with increasing calcination temperature the % of HAp increases while the % of β-TCP decreases. The CS increased with temperature based on Scherrer (most widely accepted) and Halder-Wagner (best fitted method with $R^2 > 0.9$) estimation. CI also increased with temperature except for CI_{XRD} and CI_{Raman} technique which may not be suitable for this approximation. The particle size based on FESEM image and the DLS hydrodynamic diameter both increased with increasing temperature. According to our investigation, variance in CS, CI and particle size have little impact on the biomedical competency of the synthesized S-HAp750, S-HAp850 and S-HAp950. All the samples were found to be highly cell viable and hemocompatible. In addition to that, the 3 weeks immersion in SBF caused the formation of apatite layer, indicating their bioactivity in physiological conditions. The

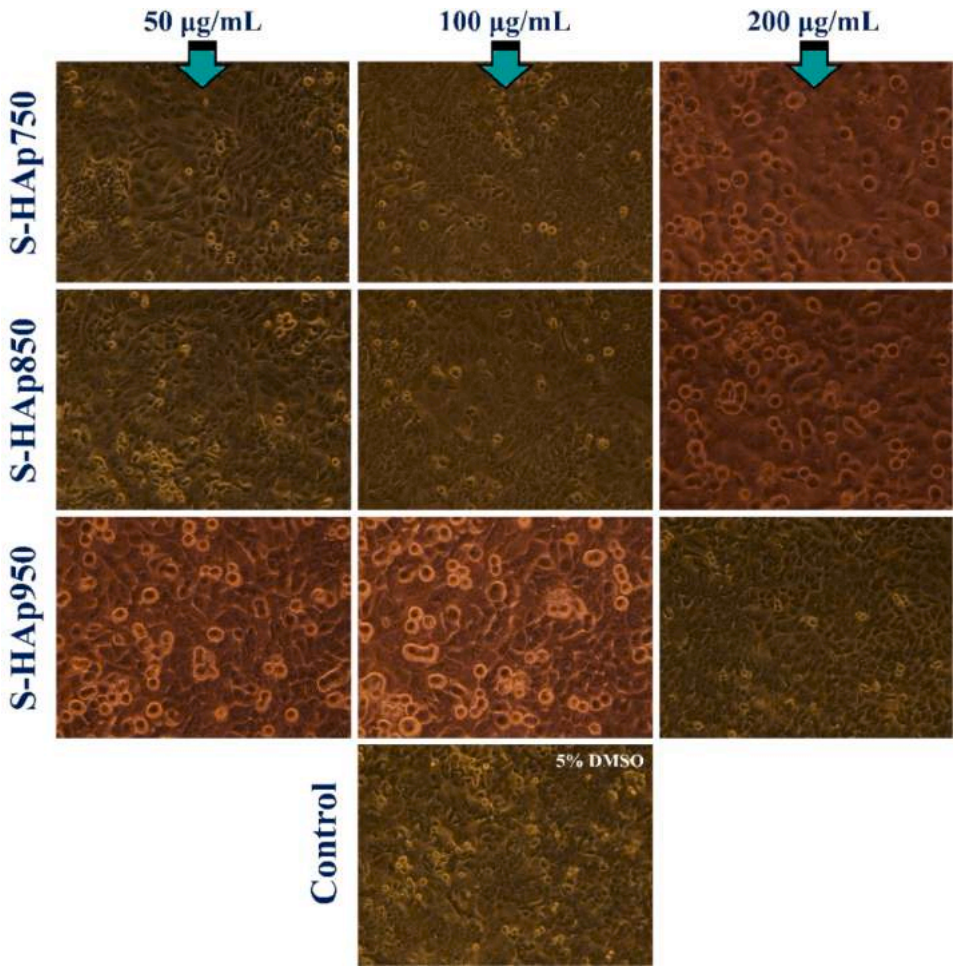

Fig. 10. Microscopic images of Vero Cell line cultured with S-HAp samples at 50, 100 and 200 µg/mL concentration and incubated for 24 h.

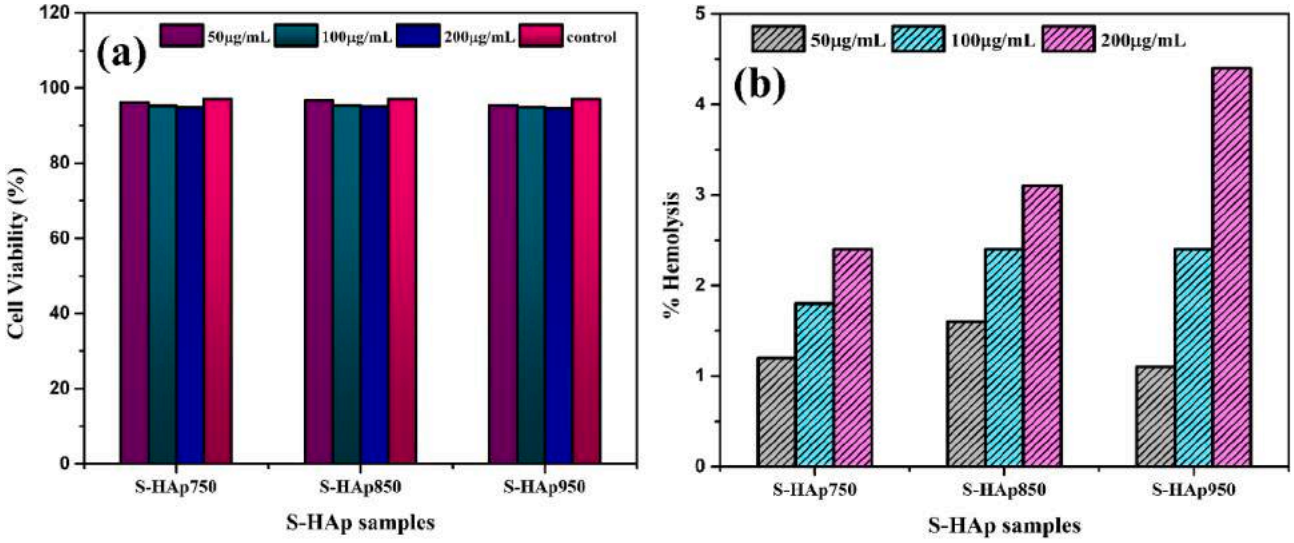

Fig. 11. (a) % of cell viability and (b) % of hemolysis of S-HAp samples at 50, 100 and 200 µg/mL concentration.

antibacterial assessment demonstrated noteworthy antibacterial effects against the gram-positive bacterium *S. aureus*, while there was no observed impact against the gram-negative bacterium *E. coli*.

Funding

Not applicable.

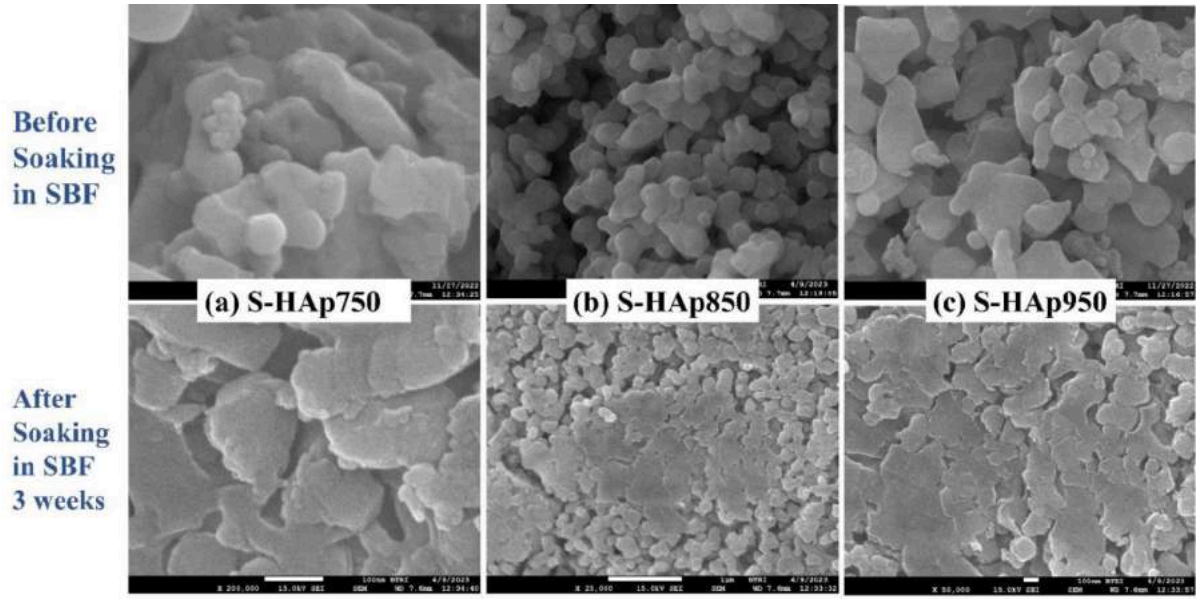

Fig. 12. Bio-activity study of S-HAp samples based on FESEM images; before and after soaking in SBF for 3 weeks: (a) S-HAp750, (b) S-HAp850 and (c) S-HAp950.

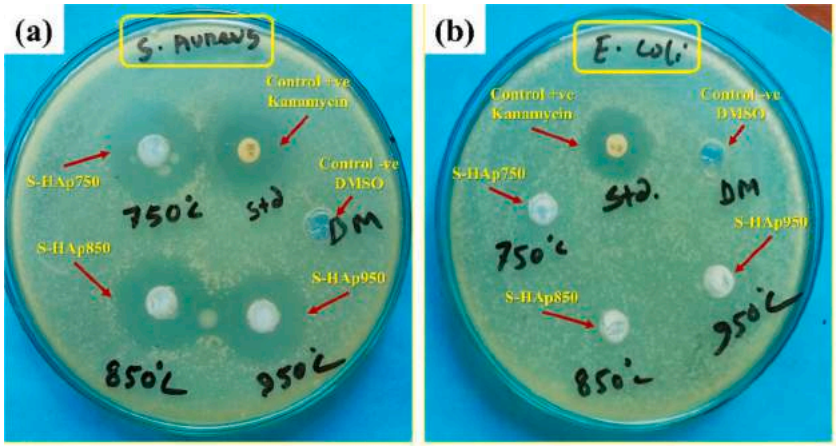

(C) Sample ID	Zone of inhibition (mm)	
	Staphylococcus aureus (ATCC 9144)	*Escherichia coli* (ATCC 11303)
S-HAp750	26	-
S-HAp850	26	-
S-HAp950	24	-
Positive Control (Kanamycin 30μg)	18	18
Negative Control (DMSO)	-	-

Fig. 13. Antibacterial activity of S-HAp750, S-HAp850 and S-HAp950 (400 μg/ml) against (a) *Staphylococcus aureus, (b) Escherichia coli* and (c) measured zone of inhibition.

CRediT authorship contribution statement

Mashrafi Bin Mobarak: Writing – review & editing, Writing – original draft, Software, Resources, Project administration, Methodology, Investigation, Funding acquisition, Formal analysis, Data curation, Conceptualization. **Md. Najem Uddin:** Investigation, Formal analysis. **Fariha Chowdhury:** Investigation, Formal analysis. **Md. Sahadat Hossain:** Methodology, Formal analysis, Data curation. **Monika Mahmud:** Formal analysis. **Shifa Sarkar:** Methodology, Formal analysis. **Nazmul Islam Tanvir:** Formal analysis. **Samina Ahmed:** Supervision, Resources, Funding acquisition.

Declaration of Competing Interest

The authors declare that they have no known competing financial interests or personal relationships that could have appeared to influence the work reported in this paper

Data availability

Data will be made available on request.

Acknowledgement

The authors are gratefully acknowledging Bangladesh Council of Scientific and Industrial Research (BCSIR) authority for supporting through R&D project (Ref. no. 39.02.0000.011.14.134.2021/900; Date: 30.12.2021). Part of this work was supported by Ministry of Science and Technology, People's Republic of Bangladesh through the special allocation project (Ref. no: 39.00.0000.009.99.024.22-901- SRG-222378; Date: 14/11/2022). We are thankful for the support from IGCRT, Dhaka Lab, BTRI and CARF.

References

[1] V. Uskoković, D.P. Uskoković, Nanosized hydroxyapatite and other calcium phosphates: chemistry of formation and application as drug and gene delivery agents, J. Biomed. Mater. Res. B 96 (2011) 152–191.
[2] F.H. Albee, Studies in bone growth: triple calcium phosphate as a stimulus to osteogenesis, Ann. Surg. 71 (1920) 32.
[3] C.S. Chai, B. Ben-Nissan, Bioactive nanocrystalline sol–gel hydroxyapatite coatings, J. Mater. Sci. Mater. Med. 10 (1999) 465–469.
[4] G. Heness, B. Ben-Nissan, Innovative bioceramics, Mater. Forum 27 (2004) 104–114.

[5] V.G. DileepKumar, M.S. Sridhar, P. Aramwit, V.K. Krut'ko, O.N. Musskaya, I. E. Glazov, N. Reddy, A review on the synthesis and properties of hydroxyapatite for biomedical applications, J. Biomater. Sci. Polym. Ed. 33 (2022) 229–261.

[6] A.S. Posner, A. Perloff, A.F. Diorio, Refinement of the hydroxyapatite structure, Acta Crystallogr. 11 (1958) 308–309.

[7] M.H. Fathi, A. Hanifi, V. Mortazavi, Preparation and bioactivity evaluation of bone-like hydroxyapatite nanopowder, J. Mater. Process. Technol. 202 (2008) 536–542.

[8] D.G. Filip, V.-A. Surdu, A.V. Paduraru, E. Andronescu, Current development in biomaterials—Hydroxyapatite and bioglass for applications in biomedical field: a review, J. Funct. Biomater. 13 (2022) 248.

[9] D.S. Gomes, A.M.C. Santos, G.A. Neves, R.R. Menezes, A brief review on hydroxyapatite production and use in biomedicine, Cerâmica 65 (2019) 282–302.

[10] L.O. Ahmed, N. Bulut, F. Osmanlıoğlu, B. Tatar, H. Kebiroglu, T. Ates, S. Koytepe, B. Ates, S. Keser, O. Kaygili, Theoretical and experimental investigation of the effects of Pr dopant on the electronic band structure, thermal, structural, in vitro biocompatibility of Er-based hydroxyapatites, J. Mol. Struct. 1280 (2023), 135095.

[11] O.P. Oni, Y. Hu, S. Tang, H. Yan, H. Zeng, H. Wang, L. Ma, C. Yang, J. Ran, Syntheses and applications of mesoporous hydroxyapatite: a review, Mater. Chem. Front.7 (2023) 9–43.

[12] M.B. Mobarak, N.S. Pinky, F. Chowdhury, M.S. Hossain, M. Mahmud, M.S. Quddus, S.A. Jahan, S. Ahmed, Environmental remediation by hydroxyapatite: solid state synthesis utilizing waste chicken eggshell and adsorption experiment with Congo Red Dye, J. Saudi Chem. Soc. 27 (2023) 101690.

[13] M.B. Mobarak, M.S. Hossain, Z. Yeasmin, M. Mahmud, M.M. Rahman, S. Sultana, S. M. Masum, S. Ahmed, Probing the photocatalytic competency of hydroxyapatite synthesized by solid state and wet chemical precipitation method, J. Mol. Struct. 1252 (2022), 132142.

[14] M. Sadat-Shojai, M.-T. Khorasani, E. Dinpanah-Khoshdargi, A. Jamshidi, Synthesis methods for nanosized hydroxyapatite with diverse structures, Acta Biomater. 9 (2013) 7591–7621.

[15] A. Yelten-Yilmaz, S. Yilmaz, Wet chemical precipitation synthesis of hydroxyapatite (HA) powders, Ceram. Int. 44 (2018) 9703–9710.

[16] G. Bezzi, G. Celotti, E. Landi, T.M.G. La Torretta, I. Sopyan, A. Tampieri, A novel sol–gel technique for hydroxyapatite preparation, Mater. Chem. Phys. 78 (2003) 816–824.

[17] J. Liu, X. Ye, H. Wang, M. Zhu, B. Wang, H. Yan, The influence of pH and temperature on the morphology of hydroxyapatite synthesized by hydrothermal method, Ceram. Int. 29 (2003) 629–633.

[18] S. Pramanik, A.K. Agarwal, K.N. Rai, A. Garg, Development of high strength hydroxyapatite by solid-state-sintering process, Ceram. Int. 33 (2007) 419–426.

[19] M.N. Hassan, M.M. Mahmoud, A. Abd El-Fattah, S. Kandil, Microwave-assisted preparation of nano-hydroxyapatite for bone substitutes, Ceram. Int. 42 (2016) 3725–3744.

[20] S. Sultana, M.S. Hossain, M. Mahmud, M.B. Mobarak, M.H. Kabir, N. Sharmin, S. Ahmed, UV-assisted synthesis of hydroxyapatite from eggshells at ambient temperature: cytotoxicity, drug delivery and bioactivity, RSC Adv. 11 (2021) 3686–3694.

[21] M.S. Hossain, M.A.A. Shaikh, S.A. Jahan, M. Mahmud, M.B. Mobarak, M. S. Rahaman, M.N. Uddin, S. Ahmed, Exploring the biomedical competency of gamma-radiation aided hydroxyapatite and its composite fabricated with nano-cellulose and chitosan, RSC Adv. 13 (2023) 9654–9664.

[22] X. Guo, H. Yan, S. Zhao, Z. Li, Y. Li, X. Liang, Effect of calcining temperature on particle size of hydroxyapatite synthesized by solid-state reaction at room temperature, Adv. Powder Technol. 24 (2013) 1034–1038.

[23] I.R. Oliveira, T.L. Andrade, K. Araujo, A.P. Luz, V.C. Pandolfelli, Hydroxyapatite synthesis and the benefits of its blend with calcium aluminate cement, Ceram. Int. 42 (2016) 2542–2549.

[24] NAS Mohd Pu'ad, P Koshy, HZ Abdullah, MI Idris, TC Lee, Syntheses of hydroxyapatite from natural sources, Heliyon 5 (5) (2019), e01588.

[25] A.M. Castillo-Paz, S.M. Londoño-Restrepo, C. Ortiz-Echeverri, R. Ramirez-Bon, M. E. Rodriguez-García, Physicochemical properties of 3D bovine natural scaffolds as a function of the anterior-posterior, lateral and superior-inferior directions, Materialia 16 (2021), 101100.

[26] O.M. Gomez-Vazquez, B.A. Correa-Piña, L.F. Zubieta-Otero, A.M. Castillo-Paz, S. M. Londoño-Restrepo, M.E. Rodriguez-García, Synthesis and characterization of bioinspired nano-hydroxyapatite by wet chemical precipitation, Ceram. Int. 47 (2021) 32775–32785.

[27] M. Waheed, M. Yousaf, A. Shehzad, M. Inam-Ur-Raheem, M.K.I. Khan, M.R. Khan, N. Ahmad, R.M. Aadil, Channelling eggshell waste to valuable and utilizable products: a comprehensive review, Trends Food Sci. Technol. 106 (2020) 78–90.

[28] M. Hossain, M. Mahmud, M.B. Mobarak, S. Ahmed, Crystallographic analysis of biphasic hydroxyapatite synthesized by different methods: an appraisal between new and existing models, Chem. Pap. 76 (2022) 1593–1605.

[29] M. Hossain, M. Mahmud, M.B. Mobarak, S. Sultana, M. Shaikh, A. Ali, S. Ahmed, New analytical models for precise calculation of crystallite size: application to synthetic hydroxyapatite and natural eggshell crystalline materials, Chem. Pap. 76 (2022) 7245–7251.

[30] M. Bin Mobarak, Md.S. Hossain, F. Chowdhury, S. Ahmed, Synthesis and characterization of CuO nanoparticles utilizing waste fish scale and exploitation of XRD peak profile analysis for approximating the structural parameters, Arab. J. Chem. 15 (2022), 104117, https://doi.org/10.1016/j.arabjc.2022.104117.

[31] A. Monshi, M.R. Foroughi, M.R. Monshi, Modified Scherrer equation to estimate more accurately nano-crystallite size using XRD, World J. Nano Sci. Eng. 2 (2012) 154–160.

[32] D. Nath, F. Singh, R. Das, X-ray diffraction analysis by Williamson–Hall, Halder–Wagner and size-strain plot methods of CdSe nanoparticles-a comparative study, Mater. Chem. Phys. 239 (2020), 122021.

[33] V.D. Mote, Y. Purushotham, B.N. Dole, Williamson–Hall analysis in estimation of lattice strain in nanometer-sized ZnO particles, J. Theor. Appl Phys. 6 (2012) 1–8.

[34] J. Reyes-Gasga, E.L. Martínez-Piñeiro, G. Rodríguez-Álvarez, G.E. Tiznado-Orozco, R. García-García, E.F. Brès, XRD and FTIR crystallinity indices in sound human tooth enamel and synthetic hydroxyapatite, Mater. Sci. Eng. C. 33 (2013) 4568–4574.

[35] Y. Sa, Y. Guo, X. Feng, M. Wang, P. Li, Y. Gao, X. Yang, T. Jiang, Are different crystallinity-index-calculating methods of hydroxyapatite efficient and consistent? New J. Chem. 41 (2017) 5723–5731.

[36] A.C. Tas, Synthesis of biomimetic Ca-hydroxyapatite powders at 37 C in synthetic body fluids, Biomaterials 21 (2000) 1429–1438.

[37] W. Strober, Trypan blue exclusion test of cell viability, Curr. Protoc. Immunol. 21 (1997) A–3B.

[38] V.P. Padmanabhan, S.N. TSN, S. Sagadevan, M.E. Hoque, R. Kulandaivelu, Advanced lithium substituted hydroxyapatite nanoparticles for antimicrobial and hemolytic studies, New J. Chem. 43 (2019) 18484–18494.

[39] R. Yang, R. Wang, S. Abbaspoor, M. Rajan, A.T. Jalil, M.M. Saleh, W. Wang, In vitro and in vivo evaluation of hydrogel-based scaffold for bone tissue engineering application, Arab. J. Chem. 16 (2023), 104799.

[40] T. Saha, M.B. Mobarak, M.N. Uddin, M.S. Quddus, M.R. Naim, N.S. Pinky, Biogenic synthesis of copper oxide (CuO) NPs exploiting Averrhoa carambola leaf extract and its potential antibacterial activity, Mater. Chem. Phys. 305 (2023), 127979.

[41] D. Brazete, J.C.C. Abrantes, J.M.F. Ferreira, Influence of the Ca/P ratio and cooling rate on the allotropic α ↔ β-tricalcium phosphate phase transformations, Ceram. Int. 44 (2018) 8249–8256.

[42] I. Mobasherpour, M.S. Heshajin, A. Kazemzadeh, M. Zakeri, Synthesis of nanocrystalline hydroxyapatite by using precipitation method, J. Alloys Compd. 430 (2007) 330–333.

[43] O. Jongprateep, N. Jitanukul, K. Saphongxay, B. Petchareanmongkol, A. Bansiddhi, A. Laobuthee, A. Lertworasirikul, R. Techapiesancharoenkij, Hydroxyapatite coating on an aluminum/bioplastic scaffold for bone tissue engineering, RSC Adv 12 (2022) 26789–26799.

[44] P.R. Prezas, M.J. Soares, J.P. Borges, J.C. Silva, F.J. Oliveira, M.P.F. Graça, Bioactivity enhancement of plasma-sprayed hydroxyapatite coatings through non-contact corona electrical charging, Nanomaterials 13 (2023) 1058.

[45] S.M. Londoño-Restrepo, B.M. Millán-Malo, A. del Real-López, M.E. Rodriguez-García, In situ study of hydroxyapatite from cattle during a controlled calcination process using HT-XRD, Mater. Sci. Eng. C. 105 (2019), 110020.

[46] W. Hui, Y. Xu, F. Xia, H. Lu, B. Li, L. Chao, T. Niu, B. Du, H. Du, X. Ran, In situ observation of δ phase suppression by lattice strain in all-inorganic perovskite solar cells, Nano Energy 73 (2020), 104803.

[47] W. Wijesinghe, M. Mantilaka, E.V.A. Premalal, H. Herath, S. Mahalingam, M. Edirisinghe, R. Rajapakse, R.M.G. Rajapakse, Facile synthesis of both needle-like and spherical hydroxyapatite nanoparticles: effect of synthetic temperature and calcination on morphology, crystallite size and crystallinity, Mater. Sci. Eng. C. 42 (2014) 83–90.

[48] P. Moghimian, A. Najafi, S. Afshar, J. Javadpour, Effect of low temperature on formation mechanism of calcium phosphate nano powder via precipitation method, Adv. Powder Technol. 23 (2012) 744–751.

[49] N.K. Nga, N.T.T. Chau, P.H. Viet, Facile synthesis of hydroxyapatite nanoparticles mimicking biological apatite from eggshells for bone-tissue engineering, Colloids Surf. B 172 (2018) 769–778.

[50] G. Montes-Hernandez, F. Renard, Nucleation of brushite and hydroxyapatite from amorphous calcium phosphate phases revealed by dynamic in situ Raman spectroscopy, J. Phys. Chem. C. 124 (2020) 15302–15311.

[51] P.E. Timchenko, E.V. Timchenko, E.V. Pisareva, M.Y. Vlasov, L.T. Volova, O. O. Frolov, A.R. Kalimullina, Experimental studies of hydroxyapatite by Raman spectroscopy, J. Opt. Technol. 85 (2018) 130–135.

[52] U. Anjaneyulu, D.K. Pattanayak, U. Vijayalakshmi, Snail shell derived natural hydroxyapatite: effects on NIH-3T3 cells for orthopedic applications, Mater. Manuf. Process. 31 (2016) 206–216.

[53] V.P. Padmanabhan, R. Kulandaivelu, D.S. Panneer, S. Vivekananthan, S. Sagadevan, J.A. Lett, Microwave synthesis of hydroxyapatite encumbered with ascorbic acid intended for drug leaching studies, Mater. Res. Innov. 24:3 (2019) 171-178.

[54] A. Gupta, A. Prasad, N. Mulchandani, M. Shah, M.Ravi Sankar, S. Kumar, V. Katiyar, Multifunctional nanohydroxyapatite-promoted toughened high-molecular-weight stereocomplex poly (lactic acid)-based bionanocomposite for both 3D-printed orthopedic implants and high-temperature engineering applications, ACS Omega 2 (2017) 4039–4052.

[55] A. Anwar, Q. Kanwal, S. Akbar, A. Munawar, A. Durrani, M.H. Farooq, Synthesis and characterization of pure and nanosized hydroxyapatite bioceramics, Nanotechnol. Rev. 6 (2017) 149–157.

[56] J. Xue, A. Farris, Y. Wang, W. Yeh, C. Romany, J.K. Guest, W.L. Grayson, A.S. Hall, T.P. Weihs, Electrodeposition of hydroxyapatite on a metallic 3D-woven bioscaffold, Coatings 10 (2020) 715.

[57] A. Bishnoi, S. Kumar, N. Joshi, Wide-angle X-ray diffraction (WXRD): technique for characterization of nanomaterials and polymer nanocomposites. Microsc. Methods Nanomater. Charact., Elsevier, 2017, pp. 313–337.

[58] V. Uvarov, I. Popov, Metrological characterization of X-ray diffraction methods for determination of crystallite size in nano-scale materials, Mater. Charact. 58 (2007) 883–891.

[59] M. Hossain, M. Hasan, M. Mahmud, M.B. Mobarak, S. Ahmed, Assessment of crystallite size of UV-synthesized hydroxyapatite using different model equations, Chem. Pap. 77 (2023) 463–471.
[60] A.M. Castillo-Paz, S.M. Londoño-Restrepo, L. Tirado-Mejía, M.A. Mondragón, M. E. Rodríguez-García, Nano to micro size transition of hydroxyapatite in porcine bone during heat treatment with low heating rates, Prog. Nat. Sci. Mater. Int. 30 (2020) 494–501.
[61] A.M. Castillo-Paz, M. Gomez-Resendiz, D.F. Cañon-Davila, B.A. Correa-Piña, R. Ramírez-Bon, M.E. Rodriguez-Garcia, The effect of temperature on the physical-chemical properties of bovine hydroxyapatite biomimetic scaffolds for bone tissue engineering, Ceram. Int. 49 (2023) 33735–33747.
[62] D.F. Cañon-Davila, A.M. Castillo-Paz, S.M. Londoño-Restrepo, H. Pfeiffer, R. Ramirez-Bon, M.E. Rodriguez-Garcia, Study of the coalescence phenomena in biogenic nano-hydroxyapatite produced by controlled calcination processes at low temperature, Ceram. Int. 49 (2023) 17524–17533.
[63] N. Pleshko, A. Boskey, R. Mendelsohn, Novel infrared spectroscopic method for the determination of crystallinity of hydroxyapatite minerals, Biophys. J. 60 (1991) 786–793.
[64] I.S. Neira, F. Guitián, T. Taniguchi, T. Watanabe, M. Yoshimura, Hydrothermal synthesis of hydroxyapatite whiskers with sharp faceted hexagonal morphology, J. Mater. Sci. 43 (2008) 2171–2178.
[65] K. Suttiponparnit, J. Jiang, M. Sahu, S. Suvachittanont, T. Charinpanitkul, P. Biswas, Role of surface area, primary particle size, and crystal phase on titanium dioxide nanoparticle dispersion properties, Nanoscale Res Lett. 6 (2011) 1–8.
[66] T. Groth, P. Falck, R.-R. Miethke, Cytotoxicity of biomaterials—Basic mechanisms and in vitro test methods: a review, Altern. Lab. Anim. 23 (1995) 790–799.
[67] A. Jayakumar, S. Radoor, J.W. Rhim, J. Parameswaranpillai, S. Siengchin, J. T. Kim, Cytotoxicity and biocompatibility of biobased materials. Adv. Appl. Biobased Mater., Elsevier, 2023, pp. 533–547.
[68] I.O. for Standardization, ISO 10993-5: 2009-Biological evaluation of medical devices-Part 5: tests for in vitro cytotoxicity, (2009).
[69] C. Sperling, M.F. Maitz, C. Werner, Test methods for hemocompatibility of biomaterials. Hemocompatibility Biomater. Clin. Appl., Elsevier, 2018, pp. 77–104.
[70] V. Sarath Chandra, G. Baskar, R.V. Suganthi, K. Elayaraja, M.I. Ahymah Joshy, W. Sofi Beaula, R. Mythili, G. Venkatraman, S. Narayana Kalkura, Blood compatibility of iron-doped nanosize hydroxyapatite and its drug release, ACS Appl. Mater. Interfaces 4 (2012) 1200–1210.
[71] S.-L. Bee, Y. Bustami, A. Ul-Hamid, K. Lim, Z.A. Abdul Hamid, Synthesis of silver nanoparticle-decorated hydroxyapatite nanocomposite with combined bioactivity and antibacterial properties, J. Mater. Sci. Mater. Med. 32 (2021) 106.
[72] M.S. Hossain, M.N. Uddin, S. Sarkar, S. Ahmed, Crystallographic dependency of waste cow bone, hydroxyapatite, and β-tricalcium phosphate for biomedical application, J. Saudi Chem. Soc. 26 (2022), 101559.
[73] G.S. Kumar, S. Rajendran, S. Karthi, R. Govindan, E.K. Girija, G. Karunakaran, D. Kuznetsov, Green synthesis and antibacterial activity of hydroxyapatite nanorods for orthopedic applications, MRS Commun. 7 (2017) 183–188.
[74] S. Lamkhao, M. Phaya, C. Jansakun, N. Chandet, K. Thongkorn, G. Rujijanagul, P. Bangrak, C. Randorn, Synthesis of hydroxyapatite with antibacterial properties using a microwave-assisted combustion method, Sci. Rep. 9 (2019) 4015.
[75] N. Kavanagh, E.J. Ryan, A. Widaa, G. Sexton, J. Fennell, S. O'Rourke, K.C. Cahill, C.J. Kearney, F.J. O'Brien, S.W. Kerrigan, Staphylococcal osteomyelitis: disease progression, treatment challenges, and future directions, Clin. Microbiol. Rev. 31 (2018) e00084-17.
[76] U. Joosten, A. Joist, G. Gosheger, U. Liljenqvist, B. Brandt, C. von Eiff, Effectiveness of hydroxyapatite-vancomycin bone cement in the treatment of Staphylococcus aureus induced chronic osteomyelitis, Biomaterials 26 (2005) 5251–5258.